The Astrophysical Journal, 764:126 (8pp), 2013 February 20 doi:10.1088/0004-637X/764/2/126

THE ROLE OF PRESSURE ANISOTROPY ON PARTICLE ACCELERATION DURING MAGNETIC RECONNECTION

K. M. Schoeffler[1], J. F. Drake[1], M. Swisdak[1], and K. Knizhnik[2]
[1] Institute for Research in Electronics and Applied Physics, University of Maryland, College Park, MD 20742-3511, USA
[2] Department of Physics and Astronomy, Johns Hopkins University, Baltimore, MD 21218-2686, USA
Received 2012 May 8; accepted 2012 December 23; published 2013 January 31

ABSTRACT

Voyager spacecraft observations have revealed that contrary to expectations, the source of anomalous cosmic rays (ACRs) is not at the local termination shock. A possible mechanism of ACR acceleration is magnetic reconnection in the heliosheath. Using a particle-in-cell code, we investigate the effects of β on reconnection-driven particle acceleration by studying island growth in multiple interacting Harris current sheets. Many islands are generated, and particles are dominantly heated through Fermi reflection in contracting islands during island growth and merging. There is a striking difference between the heating of electrons versus the heating of ions. There is a strong dependence of β on electron heating, while the ion heating is insensitive to β. Anisotropies develop with $T_\parallel \neq T_\perp$ for both electrons and ions. The electron anisotropies support the development of a Weibel instability that suppresses the Fermi acceleration of the electrons. Since the Weibel instability develops at a larger $T_\parallel/T_\perp$ in lower β systems, electrons are able to accelerate more efficiently by the Fermi mechanism at low β. The variance in anisotropy implies less electron acceleration in higher β systems, and thus less heating. This study sheds light on particle acceleration mechanisms within the sectored magnetic field regions of the heliosheath and the dissipation of turbulence such as that produced by the magnetorotational instability in accreting systems.

Key words: magnetic reconnection – methods: numerical – plasmas – Sun: general – Sun: heliosphere

Online-only material: color figures

1. INTRODUCTION

Energetic particles are often associated with magnetic reconnection. Their presence is inferred from observations (Lin et al. 2003) of gamma rays and X-rays that are generated by the collisions of accelerated electrons and ions with the solar atmosphere (Lin et al. 2003). Direct detections of energetic electrons in reconnection outflows have been made in the magnetotail (Øieroset et al. 2002). When reconnection occurs, many magnetic islands can form. This can be seen in observations of flux transfer events in the magnetopause (Russell & Elphic 1979), bursty bulk flows in the magnetotail (Slavin et al. 1993), and in supra-arcade downflows in the solar corona (Sheeley et al. 2004; McKenzie & Savage 2009; Savage et al. 2012). Energization through a mechanism of Fermi reflection within islands was suggested by Kliem (1994), and later Drake et al. (2006). Recent simulations have revealed energization through this Fermi mechanism in particle-in-cell (PIC) models (Oka et al. 2010; Drake et al. 2010; Schoeffler et al. 2011) as well as in test particle studies in magnetohydrodynamic (MHD) models (Kowal et al. 2011, 2012). Reconnection has been suggested as a source for the anomalous cosmic rays found in the heliosheath (Lazarian & Opher 2009; Drake et al. 2010).

An effective method for examining the energization of particles is to simulate several stacked current sheets, which leads to large numbers of interacting magnetic islands. This method is particularly relevant to the sectored magnetic fields found in the low-latitude heliosheath (Drake et al. 2010; Czechowski et al. 2010). In the high β regime found in the heliosheath, the pressure anisotropy prevents magnetic islands from fully contracting and as a result, islands at late time retain large aspect ratios (Schoeffler et al. 2011). We implement this system in a two-dimensional PIC code, and vary the temperature of the background plasma to test the dependence on β, where β is the ratio of plasma pressure (ion plus electron) to the magnetic pressure. A PIC simulation allows us to investigate the effects of pressure anisotropy on particle acceleration. However, due to computational constraints, we only explore systems with two space dimensions.

Once islands develop, they begin to contract, simultaneously accelerating particles via a first-order Fermi process. This process is analogous to a ball bouncing between two inwardly moving walls. Each time the ball (ion or electron) collides with a wall (the magnetic edge of an island), it gains energy. One of the signatures of first-order Fermi acceleration is that the energy gain of a particle is proportional to energy. In the case of particles bouncing in a magnetic island, the energy gain occurs in the parallel velocity of the particle and leads to temperature anisotropies with $T_\parallel > T_\perp$. Two competing instabilities, Weibel (Weibel 1959) and fire hose (Parker 1958), can be generated by such an anisotropy.

The particle acceleration due to the Fermi mechanism should, in principle, depend on β (Drake et al. 2006, 2010). The Fermi mechanism accelerates particles in the direction parallel to the magnetic field and thus creates a pressure anisotropy. As the anisotropy grows, the system approaches marginal fire-hose stability, where the tension of the bent magnetic fields, and along with it the Alfvén speed, reduces to zero. The fire-hose instability occurs when

$$1 - \frac{\beta_\parallel - \beta_\perp}{2} > 0.$$

Particles gain energy in the Fermi mechanism by reflecting from the ends of islands contracting at the Alfvén speed, where the contraction is driven by magnetic tension. As tension decreases, the outflow velocity from the X-line is reduced and acceleration decreases as well. In higher β systems, a smaller anisotropy is needed before reaching the fire-hose stability boundary and thus

particle acceleration should be inhibited. The reduction of the outflow speed, however, plays less of a role than expected on the β dependence of acceleration. The tension of the fields goes to zero in some regions, but the regions where the tension is still large continue to contract at the Alfvén speed.

We find that the more important factor for systems with no ambient out-of-plane guide field is the development of another anisotropy instability driven by electrons, the Weibel instability. The Weibel instability develops in the presence of a temperature anisotropy in regions with near zero magnetic field and produces magnetic fields from the free energy contained in the pressure anisotropy of the unmagnetized plasma. In reconnection simulations, an instability associated with the Weibel instability can develop (Lu et al. 2011). Weibel-produced magnetic fields develop in the out-of-plane direction. These fields can scatter electrons, which isotropizes the electron temperature and disrupts the Fermi reflection process and associated energy gain.

We find that β has a strong effect on the electrons, while ion acceleration is nearly independent of β, within the range of β studied. Both the electrons and the ions are accelerated mostly by the Fermi mechanism in contracting islands. The electrons, however, stop accelerating due to the onset of the Weibel instability. The out-of-plane magnetic fields generated by the Weibel instability keep the electrons from freely bouncing back and forth and Fermi accelerating. Since the ion gyroradius is large compared to the length scales of the Weibel-generated fluctuations of the magnetic field, ions are not significantly affected by this instability.

In this paper, we first describe the computational model and the parameters used in our simulations. Next, we show individual tracked particles accelerating and eventually interacting with the Weibel magnetic fields. In addition, we show the development of the Weibel instability in the simulations along with the confirmation of the signatures of the Weibel instability in small test simulations. Finally, we draw some conclusions about what this means for real systems such as the heliosheath and accretion flows.

2. COMPUTATIONAL MODEL

Our initial setup is convenient for examining the growth of many islands and how particles can be accelerated in this context, and is based on the simulations presented previously (Schoeffler et al. 2011). Our simulations are performed with the PIC code p3d. The initial conditions consist of eight Harris current sheets (Harris 1962), where the magnetic pressure balances the plasma pressure. Each Harris sheet consists of a magnetic field profile $\mathbf{B} = B_0 \tanh(y/w_0)\hat{\mathbf{x}}$, and a density profile $n = n_0 \operatorname{sech}^2(y/w_0)$. In addition, there is a uniform background population with a density of $n_b = 0.2n_0$. These simulations are done in two dimensions with $\partial/\partial z = 0$, where $\hat{\mathbf{z}}$ is out of plane, parallel to the initial current. The $\hat{\mathbf{y}}$ direction corresponds to the radial direction and the $\hat{\mathbf{z}}$ direction corresponds to the northward direction in the heliosheath picture of this system.

The code uses normalized units. The timescale is normalized to the ion cyclotron time $\Omega_{\rm ci}^{-1}$. The distance scales are normalized to the ion inertial length $d_i = c/\omega_{\rm pi}$, and thus the velocity is normalized to the Alfvén speed v_A. The magnetic field is normalized to the asymptotic value for the reversed magnetic field B_0. The density is normalized to the peak value of the Harris profile, n_0. The pressure is normalized to $P_0 = n_0 m_i v_A^2 = B_0^2/4\pi$. The temperature is normalized to $T_0 = m_i v_A^2$.

In order to vary the β of these simulations, we adjust the temperature of the background population T_b. This background temperature is the same for both ions and electrons. The Harris equilibrium is used to balance the sharp change in the magnetic field strength across the current sheets, while the background represents the pick-up ions and has the greatest influence on late-time reconnection dynamics. We performed simulations for $\beta = 0.2$, 1, 2, 3, and 4.8, where β is based on the pressure in the asymptotic field with density n_b. Each simulation was advanced for a time of $120\Omega_{\rm ci}^{-1}$. A more detailed explanation of the parameters of the simulation is in Schoeffler et al. (2011), but the numbers are as follows: the time resolution, $dt = 0.004\Omega_{\rm ci}$, the grid scale resolution, $\Delta_x = \Delta_y = 0.05d_i$, the proton-to-electron mass ratio, $m_e/m_i = 1/25$, the ratio of the speed of light to the Alfvén speed, $c/c_A = 25$, and the half-width of the current sheet, $w_0 = 0.5d_i$. The temperature in the Harris sheet is $0.25T_0$ for both ions and electrons, and there is no ambient guide field.

Our full simulations track $\approx 10^9$ particles. Recording the trajectories of all of these particles is not feasible. However, we have recently made upgrades to p3d (Knizhnik et al. 2011) that allow us to track the trajectories of selected particles. We used the upgraded particle tracking code to follow the trajectories of approximately 200 of the most energetic electrons and ions (178 electrons and 275 ions) for the $\beta = 2$ run.

The simulation does not precisely describe the heliosheath but illustrates important physics that should be found there. The ion pressure in the heliosheath is much larger than the electron pressure, and thus β_e is actually quite moderate compared with that of the ions. We do not have a separate population of pick-up ions. The equilibrium magnetic field configuration in our simulation is a Harris sheet rather than the rotated field configuration (where $|B|$ is constant in a cut through the current sheet) that characterizes the heliospheric current sheet. However, the total out-of-plane flux from these layers is small because their width is very small compared with the total sector width. Thus, this flux should not significantly impact the dynamics. Future simulations tailored to the specific parameters of the heliosheath are planned.

3. PARTICLE ACCELERATION RESULTS

In our simulations, we investigate the effect of β on a system of stacked current sheets. Figure 1 shows the results of three of these simulations after magnetic islands begin to develop. The difference in the island lengths is discussed in Schoeffler et al. (2011). However, we also find that there is a β dependence on the heating of the electrons. The β dependence can be seen in the bulk change in pressure of the electrons, see Figure 2. Individual trajectories of accelerated electrons reveal a scattering mechanism that suppresses acceleration in large β systems. Out-of-plane magnetic fields generated by a Weibel instability play a role in the scattering of the electrons.

We explore the heating of the electrons and ions by looking at the average pressure of the system, P, which can be calculated by taking the trace of the pressure tensor and dividing by three. Over time, this pressure increases, which is reasonable since magnetic energy dissipates during reconnection. Strikingly, there is a big difference between the pressure gains of the ions and the electrons. The pressure gain of electrons is four times less for $\beta = 4.8$ than for $\beta = 0.2$, while the ion pressure gain, though delayed, is hardly changed. Since the number of particles is constant, average pressure gains imply average temperature gains. As seen in Figure 2, the heating of the

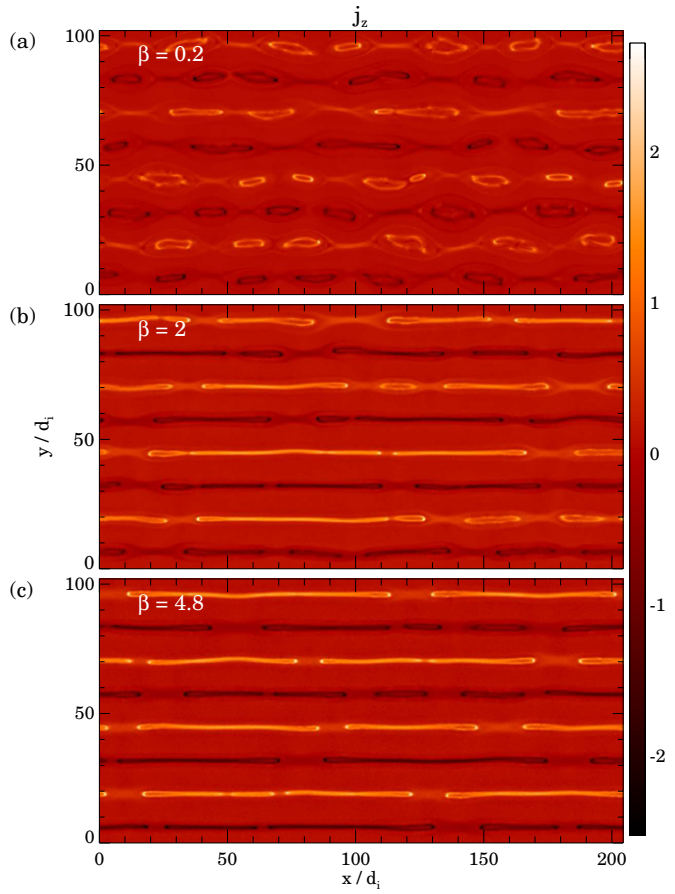

Figure 1. Out-of-plane current, j_z, at $t = 51\Omega_{ci}^{-1}$ for β of (a) 0.2, (b) 2, and (c) 4.8.

(A color version of this figure is available in the online journal.)

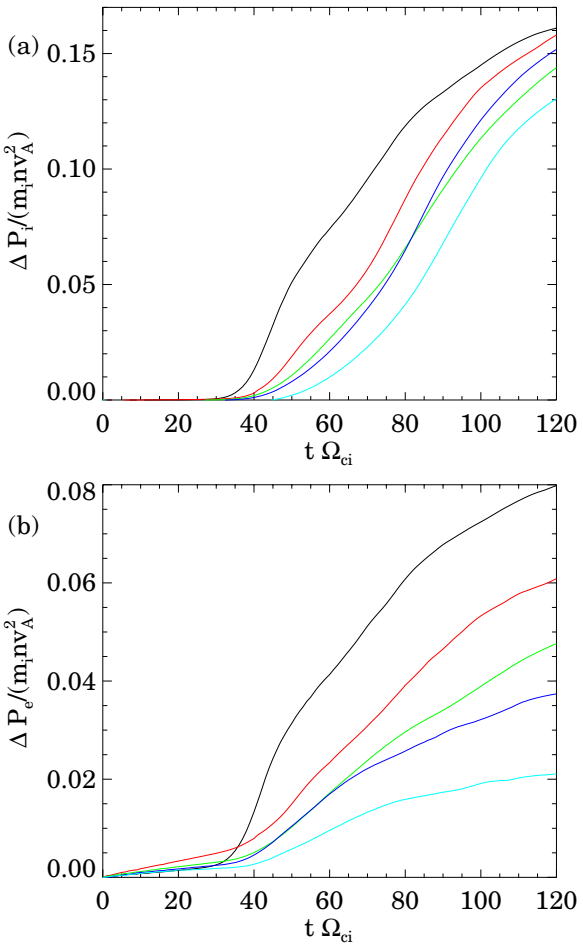

Figure 2. Change in average pressure for $\beta = 0.2$, 1, 2, 3, and 4.8 (black, red, green, blue, cyan, respectively) contained in the ions (a) and the electrons (b), where the pressure is calculated as 1/3 of the trace of the pressure tensor.

(A color version of this figure is available in the online journal.)

ions (change in average pressure from that at $t = 0$), ΔP_i, is nearly independent of β. The slight dependence observed is expected due the slowing of the outflow caused by the approach to fire-hose instability. The electron heating, ΔP_e, on the other hand is strongly dependent on β. This observation leads to the conclusion that something is occurring on the spatial scale of electrons.

We will examine the trajectory of a typical electron, but in order to understand the trajectory of the electron itself, we need to look at what the island in which the electron is located is doing. Figure 3 shows islands contracting in the $\beta = 2$ simulation for a particular current sheet. The walls of the islands move inward at Alfvénic speeds, and after $t = 60\Omega_{ci}^{-1}$ the islands begin to show evidence of the Weibel instability, which will be discussed in the next section. The electron of interest is located in the island between $x = 100$ and $150d_i$.

Figure 4 shows the trajectory of the electron. As shown in Figures 4(a) and (b), before $t = 60$, whenever the electron changes directions by bouncing off the end of the island, there is an increase in its energy. As shown in Figure 4(c), the velocity v_x along $\hat{\mathbf{x}}$ rotates to the z-direction v_z each time the bounce occurs. The $\hat{\mathbf{x}}$ direction is essentially the parallel direction, since the magnetic fields are mostly in the $\hat{\mathbf{x}}$ direction. The gain in energy is caused by the reconnection electric field which is parallel to the out-of-plane velocity during the bounce.

After the Weibel instability begins to grow around $t = 60\Omega_{ci}^{-1}$, the energy stops increasing. The structure of B_z is shown in Figure 4(e). The structures near the ends of the island at $t < 55\Omega_{ci}^{-1}$ are the first onset signature of the Weibel instability. The structure near the center of the island after $t = 55\Omega_{ci}^{-1}$ is the more developed B_z signature of the Weibel instability. The Weibel magnetic fields divert v_x, which is parallel to the reconnecting field, into v_y, which is perpendicular. The primary B_x then rotates the perpendicular velocity as the particle travels in Larmor orbits. The signature of this perpendicular velocity can be seen in v_y, shown in Figure 4(d).

Figure 5 shows the trajectory of an ion in the same island. This ion, unlike the electron, continues to gain energy throughout the time period where the Weibel instability is present. The ion acts in the same way as the electron did before $t = 60$. The higher inertia of the moving ions causes the Larmor radius to exceed the length scale of the out-of-plane Weibel field, allowing the ions to pass through without being deflected into the $\hat{\mathbf{y}}$ direction.

The trajectory shown in Figure 4 is a typical example of energetic electrons in the system. Nearly all of the tracked electrons are trapped within islands and gain energy. Many of them are deflected in a similar way. The ion in Figure 5 was chosen to be in the same island as the electron from Figure 4, but its behavior is generally similar to others in the system. Like the electrons, nearly all of the ions were trapped within islands, and gained energy.

To better understand the dependence of the heating with β, we examine the change in the average of the components of the

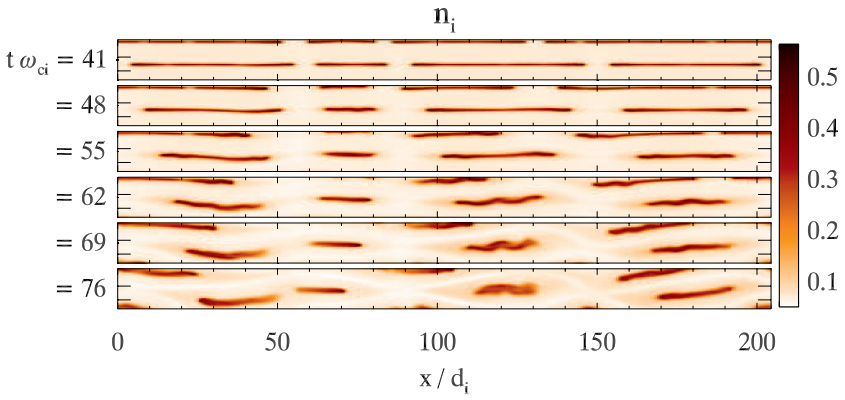

Figure 3. Ion density, n_i, for $\beta = 2$, along one current sheet between $t = 41$ and $76\Omega_{ci}^{-1}$.
(A color version of this figure is available in the online journal.)

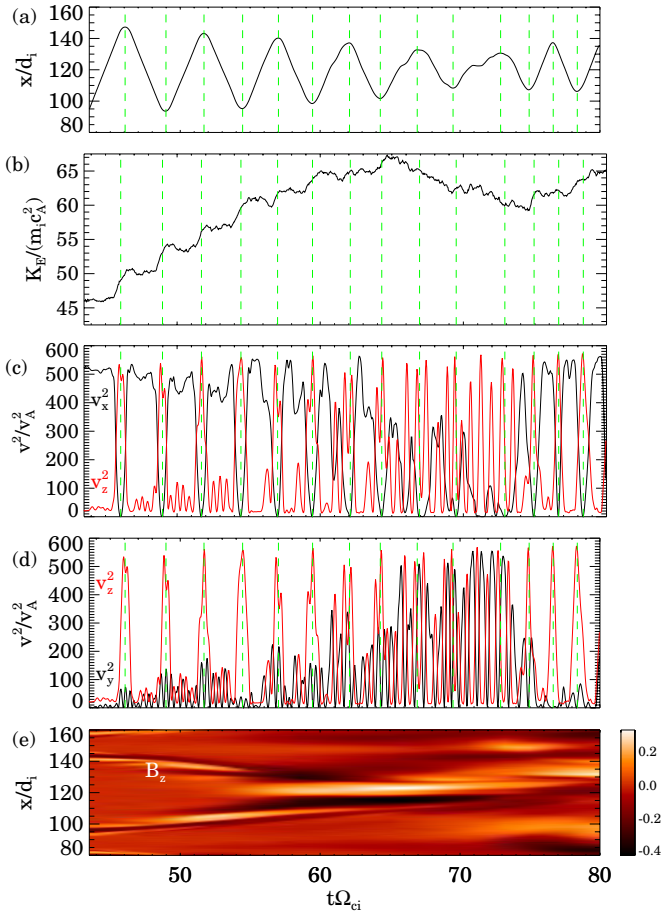

Figure 4. Trajectory of an electron; with (a) the x position vs. t, (b) the kinetic energy vs. t, (c) v_x^2 (black) and v_z^2 (red) vs. t, (d) v_y^2 (black) and v_z^2 (red) vs. t, and (e) the out-of-plane magnetic field B_z in a cut along the center of the current sheet of the island vs. t. The tracked particle is from a run with $\beta = 2, t = 43.5 - 80\Omega_{ci}^{-1}$. The green dotted lines are the times where the x velocity changes sign.
(A color version of this figure is available in the online journal.)

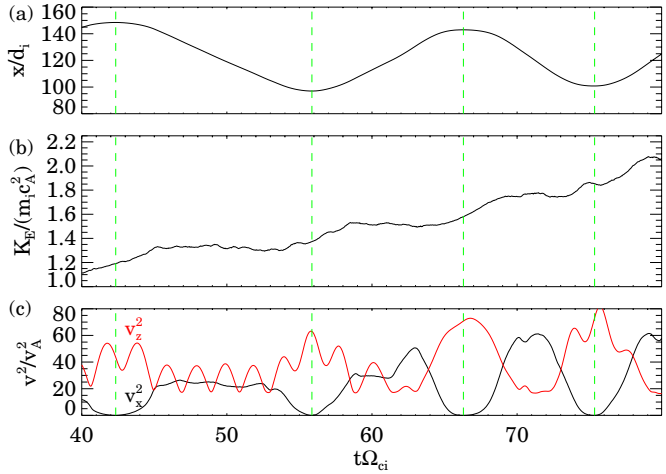

Figure 5. Trajectory of an ion; with (a) the x position vs. t, (b) the kinetic energy vs. t, and (c) v_x^2 (black) and v_z^2 (red) vs. t. The tracked particle is from a run with $\beta = 2, t = 43.5 - 80\Omega_{ci}^{-1}$. The green dotted lines are the times where the x velocity changes sign.
(A color version of this figure is available in the online journal.)

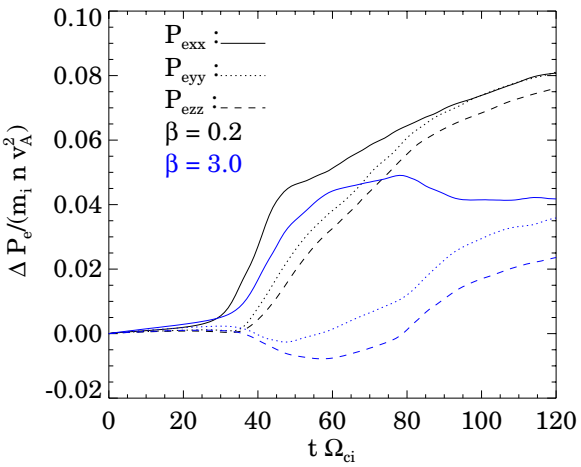

Figure 6. Change in average pressure for the electrons for $\beta = 0.2$ and 3 (black and blue, respectively), where the diagonal components of the pressure tensor are shown; P_{exx} (solid), P_{eyy} (dotted), and P_{ezz} (dashed).
(A color version of this figure is available in the online journal.)

electron pressure tensor from that at $t = 0$, ΔP_{ij}. In Figure 6, we see the growth of the pressure in the $\hat{\mathbf{x}}$ direction P_{exx} for both small and large β. Within islands where much of the temperature anisotropy develops, the magnetic field is predominantly in the $\hat{\mathbf{x}}$ direction. So again, $\hat{\mathbf{x}}$ corresponds to the parallel direction in which the Fermi process accelerates particles. In Figure 6,

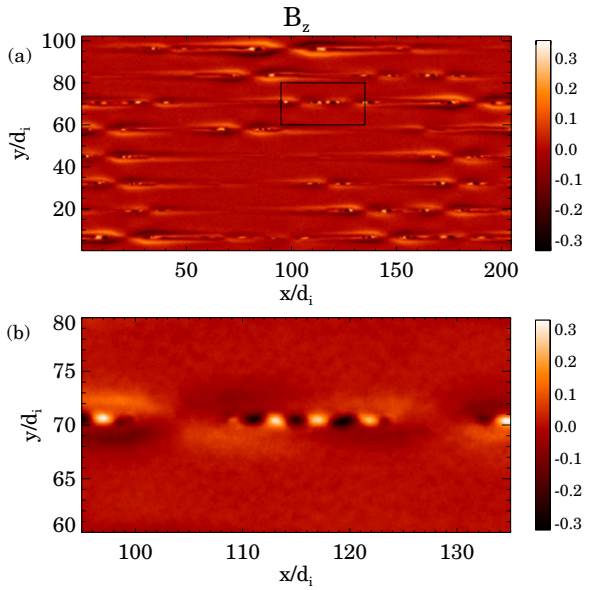

Figure 7. Out-of-plane magnetic field, B_z. Short wavelength structures are visible in the low magnetic field regions where the outflow streams through the background plasma. Zoomed in region is shown in (b). Black box in (a) indicates zoomed in region. These structures are due to a Weibel instability. This plot is taken from the $\beta = 2$ case at $t = 45\Omega_{ci}^{-1}$.

(A color version of this figure is available in the online journal.)

we see that in both low and high β, the growth of the parallel pressure significantly drops around $\Delta P_{exx} = 0.05 m_i n v_A^2$. This drop occurs at around $t = 50\Omega_{ci}^{-1}$. In each simulation, this drop in growth coincides with the onset of the Weibel instability. Although the onset is not presented for all values of β, an example of the $\beta = 2$ run is seen in Figure 4(e) for one particular island.

The Weibel instability develops for the same value of ΔP_{exx} for several values of β, two of which are shown in Figure 6. After the drop in growth of the parallel pressure, the perpendicular pressure begins to rise for all β, two of which are shown in Figure 6. This perpendicular pressure rise is due to the scattering of particles moving parallel to the magnetic field by the Weibel instability. For the $\beta = 3$ case (the blue curves in Figure 6), the scattering causes the growth of the parallel pressure to essentially stop. For $\beta = 0.2$ on the other hand, the scattering is not sufficient to completely stop the growth. This difference in scattering implies the heating of particles depends on β.

4. WEIBEL INSTABILITY

In the regions near the reconnection sites, the outflow streams through the background plasma, giving rise to an anisotropy. Anisotropies also develop within magnetic islands due to Fermi acceleration. In regions of high pressure anisotropy where the magnetic field is nearly zero, a short wavelength mode grows (Figure 7). This mode is associated with the Weibel instability. A similar Weibel instability has been found in earlier reconnection simulations (Lu et al. 2011). The region of weak magnetic field is a location where the Weibel instability is more likely to develop since the instability normally develops in an unmagnetized plasma with anisotropy. The Weibel instability has a wavevector perpendicular to the direction with higher temperature. Since the weak magnetic field region is confined above and below by magnetic fields, only half a wavelength can form. The conventional linear theory of the Weibel instability does not predict the wavevector in the $\hat{\mathbf{x}}$ direction. However, as shown in Liu et al. (2009), a wavevector along the direction of higher temperature can form such that the gyroradius associated with the magnetic field of the mode matches the wavelength. In this case, the relevant scale is the electron gyroradius. The out-of-plane magnetic field is approximately $0.3B_0$, $v_{the} \approx 8$, and $m_e = 0.04$, so the gyroradius is about $1d_i$. This is a quarter of the observed wavelength, consistent with the prediction of Liu et al. (2009).

As anisotropies grow due to the Fermi process, the entire center of the island becomes unstable to the Weibel instability. As the instability grows into the region where the magnetic field becomes significant but the length scales are still below d_i, whistler dynamics cause the out-of-plane Weibel magnetic fields to rotate into the page, causing small-scale kinking, as shown in Figure 3.

We have performed small, $25.6d_i \times 51.2d_i$, simulations with a specified initial temperature anisotropy in order to better understand the development of the Weibel instability. We use the same space and time resolution as in the larger runs. In these runs, we employ a modified Harris sheet with an initial temperature anisotropy with higher initial temperature along the $\hat{\mathbf{x}}$ direction (note that $T_\parallel$ plays no part in ensuring pressure balance, so varying it does not change the initial equilibrium). We take parameters from the late-time $\beta = 2$ simulation, where the Weibel instability develops, for which $T_b = 1.75T_0$ (see Figure 8). However, in order for the anisotropy to fully grow, the anisotropy was doubled from $T_\parallel/T_\perp = 1.76$ to 3.52. The anisotropy was initiated by varying the temperature in the parallel direction of the Harris population of both the electrons and the ions, as this is what is observed in the $\beta = 2$ reconnection simulation. Note, however, that the Weibel instability is only driven by the electron anisotropy. Finally, we performed more simulations with a variety of anisotropies, for current sheets of width $0.5d_i$ and $4.0d_i$, with both relativistic effects turned on and off. The goal was to demonstrate that the growth rate of the instability in the simulations matches that of the Weibel instability.

We have reproduced this Weibel phenomenon in our small simulation with an initial anisotropy. With the enhanced anisotropy, the instability develops until the magnetic fields kink, much like what is seen in the larger self-generated anisotropy run (Figures 8(c) and (d)).

We had to artificially increase the anisotropy in the small simulation to $\approx$3.5 in order to reproduce the Weibel phenomenon. In the $\beta = 2$ reconnection simulation, the anisotropy, $T_\parallel/T_\perp \approx 1.8$, is constantly replenished by an influx of plasma from the X-line, and Fermi acceleration. This enables the instability to grow to finite amplitude. Since the anisotropy in the test run is quickly exhausted, a much larger initial anisotropy is needed for the instability to reach large amplitude.

The instabilities found in the simulations can be identified as the Weibel instability based on an agreement with the predicted Weibel growth rates. The non-relativistic growth rate of the Weibel instability is determined from

$$k_y^2 c^2 - \omega^2 + \sum_\alpha \omega_{p\alpha}^2 \left(1 - \frac{T_{\alpha x}}{T_{\alpha y}}\right) = \sum_\alpha \omega_{p\alpha}^2 \frac{T_{\alpha x}}{T_{\alpha y}} \xi_\alpha Z(\xi_\alpha), \quad (1)$$

where

$$\xi_\alpha = \frac{\omega}{k_y \sqrt{T_{\alpha y}/m_\alpha}}, \quad (2)$$

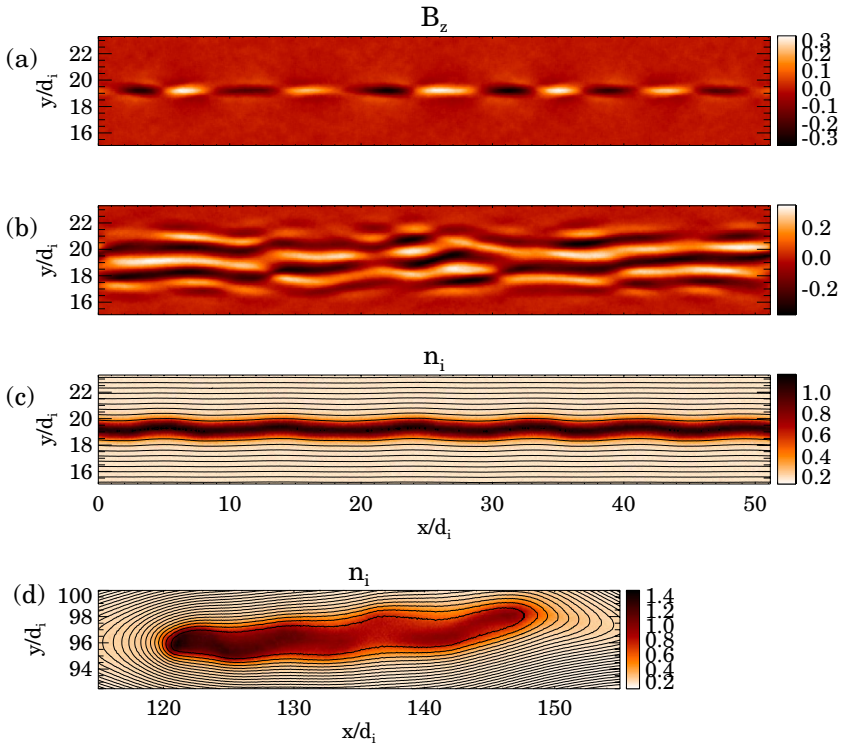

Figure 8. Panels (a)–(c) are taken from a simulation with a modified Harris sheet configuration with initial $T_{\parallel}/T_{\perp} = 3.52$. The B_z structure of the Weibel instability at $t = 0.2\Omega_{ci}^{-1}$ is shown for $w_0 =$ (a) $0.5d_i$ and (b) $4d_i$. The k_y expected from the Weibel instability is clearly visible in (b) while only half a wavelength fits in (a) and a non-zero k_x becomes evident. In (c), a kinking structure in the ion density, n_i, that appears to be an instance of the Weibel instability at $t = 5\Omega_{ci}^{-1}$ is shown, for $w_0 = 0.5d_i$. In (d) is a similar kinking structure to that seen in (c) from the $\beta = 2$ run at $t = 61\Omega_{ci}^{-1}$. The overplotted curves in (c) and (d) are contours of constant magnetic flux.

(A color version of this figure is available in the online journal.)

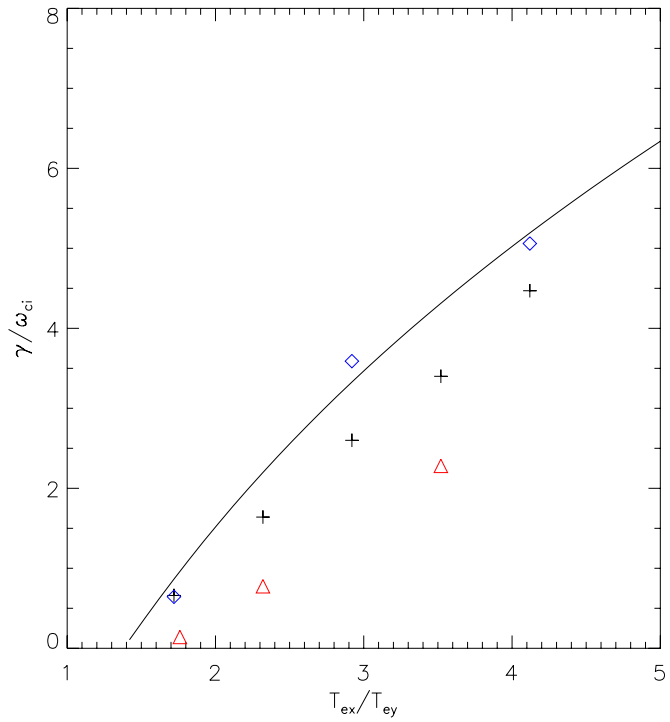

Figure 9. Growth rate vs. anisotropy, T_{ex}/T_{ey}. The black plus signs are the growth rate for $w_0 = 4d_i$. The blue diamonds have the same w_0 but the relativistic effects in the code are turned off. The red triangles are for $w_0 = 0.5d_i$. The black curve is the theoretical non-relativistic prediction for the Weibel growth rate.

(A color version of this figure is available in the online journal.)

Z is the plasma dispersion function,

$$Z(\xi_\alpha) = \frac{1}{\sqrt{\pi}} \int_{-\infty}^{\infty} \frac{\exp(-x^2)dx}{x - \xi_\alpha}, \quad (3)$$

and α is the species (Krall & Trivelpiece 1986). The growth rate is given by the imaginary part of the frequency, ω.

Since the half-width of the current sheet is smaller than the predicted wavelength of the Weibel instability, a clear wavevector along the $\hat{\mathbf{y}}$ direction is not found. To be certain we are seeing the Weibel instability, we performed a run with a current sheet half-width, $w_0 = 4d_i$. In this case, we observe several wavelengths in the $\hat{\mathbf{y}}$ direction as predicted for the Weibel instability (see Figure 8(b)). We checked the growth rate versus anisotropy and it fits very well with the predicted Weibel growth rate (Figure 9). The growth rate in Equation (1) depends on both the temperature anisotropy and the wavelength of the mode. We use the observed k_y in the comparison, although it is generally close to the maximally growing wavenumber, $k_y d_i \approx 3$. The growth rate for $w_0 = 0.5d_i$ is a bit smaller than predicted by homogeneous theory because the bounding magnetic fields suppress the growth. We also find that relativistic effects (our electrons have $v_{the}/c = 0.4$) also suppress the growth.

5. CONCLUSIONS

We find that, based on particle trajectories, first-order Fermi acceleration is the major source of energetic particle acceleration in our simulations of collisionless magnetic reconnection. Although we have shown that this is the case for the most energetic electrons, in principle, nearly all electrons that have high

enough velocities to bounce between the ends of an island during its formation will gain energy via the Fermi process. This occurs as long as the velocity is super-Alfvénic. For our simulation with $\beta = 0.2$, the electron thermal velocity $v_{\rm th} = 2.5c_A$ so that most of the electrons are energetic enough to gain energy through the Fermi process. There is a difference between the ion and electron acceleration because the ions are unaffected by the Weibel-generated magnetic fields within the islands while the electrons are scattered.

In the heliosheath, the fields are closer to a force-free configuration around the current sheet. This means that the field strength stays relatively constant rather than going to nearly zero at the center of the islands. This suggests that the Weibel instability might play a smaller role. However, since the separation between the current sheets is rather large (the ratio of the separation to the width is about 17,000 just upstream of the termination shock), the total out-of-plane flux is rather small. As the islands grow, the out-of-plane field is swept away and replaced by the anti-parallel flux. The anti-parallel flux leaves a long region with relatively small magnetic field along the current sheet where the Weibel instability can still develop.

The strongest electron scattering takes place in the magnetic field reversal region near the core of magnetic islands. However, in natural systems in which the reversal region occupies a much smaller fraction of the system domain in comparison with our simulations, the Weibel instability might play a less important role. On the other hand, in cases where the Weibel instability is suppressed, other electron instabilities such as the electron fire-hose instability should occur (Camporeale & Burgess 2008), which would also be able to scatter the electrons.

We have demonstrated that at the electron scale, anisotropy instabilities can limit the acceleration of electrons. In principle, at larger scales, ion scale instabilities such as the fire-hose instability would likely develop causing a similar effect on the ions. However, such an anisotropy also suppresses reconnection and reduces the drive for anisotropy. Thus, it is unclear whether strong fire-hose instability sufficient to scatter ions will take place. We have not yet seen significant ion scattering. On the other hand, in physical systems where the system sizes are much larger, ion scattering might take place during the much longer traversal times of magnetic islands. As long as the electrons are energetic enough by the time the ions are magnetized and begin to accelerate, we would expect these electron instabilities to take place before ion instabilities such as the standard fire-hose instability.

The dynamics of test particles were explored in MHD simulations of a similar setup of islands generated in stacked current sheets (Kowal et al. 2011, 2012) or in single current layers (Kliem 1994) reproduced the Fermi acceleration mechanism in contracting and merging islands. Thus, the basic mechanism is not a kinetic process and therefore should scale to large systems. On the other hand, particle acceleration within the Sweet–Parker-like current sheets was a significant contribution to the overall dynamics of particle acceleration in the fields from MHD simulations. Such extended current layers are unlikely to play a role in most physical systems. Either Hall effects (Shay et al. 1998), anomalous resistivity (Sato & Hayashi 1979), or ambient turbulence (Lazarian & Vishniac 1999) limits the length of current layers. Test particle modeling in MHD fields, while useful for exploring the mechanisms for acceleration, does not enable accelerated particles to back-react to the fields. Thus, calculating spectra from such models is a challenge. Finally, we have not initialized our systems with ambient turbulence (Kowal et al. 2009). In the heliosheath, such turbulence is not strong enough to significantly distort the dominantly azimuthal heliospheric magnetic field (Burlaga et al. 2006) and is therefore unlikely to facilitate reconnection there. The role that it might play in the scattering of energetic particles during reconnection is unknown and might be significant.

Due to the suppression of particle acceleration via anisotropy instabilities, we would thus expect to see a dependence of β on the energetic electrons measured from the *Voyager* spacecraft. Regions with larger β would be expected to have fewer energetic particles, since acceleration would be suppressed in that region. Three-dimensional MHD simulations of the global heliosphere (Drake et al. 2010) had suggested that the pileup of the magnetic field at the heliopause would lead to a region of low β so that the predictions of the present model could be tested. However, even though the radial flows of *Voyager 1* have dramatically decreased, no buildup of the magnetic field has been measured. A possible explanation is that reconnection is preventing the buildup of the magnetic field (Richardson et al. 2013). The unfortunate implication is that no direct comparison of particle acceleration in different β regimes will be possible with the *Voyager* measurements alone.

In accretion disks, the gravitational energy is released, and the plasma gets heated, generating radiation and energetic particles that can be measured. The gravitational energy release is proportional to the radial–azimuthal component of the stress tensor, which transports angular momentum outward and thus allows the release of gravitational energy. The stress, however, is not proportional to the increase in thermal energy. Rather, it is proportional to the magnetic energy. The generation of magnetic field energy is caused by the magnetorotational instability (MRI), which is also the source of the stress. The total magnetic field produced as a result of the release of gravitational energy by the MRI is more than three times the kinetic energy (Simon et al. 2009). Since magnetic reconnection is the dominant mechanism for releasing magnetic energy, our simulations should thus shed light on the how heating and particle acceleration develop, which would allow comparison with measurements.

Computations were performed at the National Energy Research Scientific Computing Center. This work has been supported by NSF grant AGS1202330.

REFERENCES

Burlaga, L. F., Ness, N. F., & Acuna, M. H. 2006, ApJ, 642, 584
Camporeale, E., & Burgess, D. 2008, JGR, 113, A07107
Czechowski, A., Grzedzielski, S., & Strumik, M. 2010, in AIP Conf. Proc., 1216, Twelfth International Solar Wind Conference, ed. M. Maksimovic et al. (Melville, NY: AIP) 588
Drake, J. F., Che, H., Shay, M. A., & Swisdak, M. 2006, Natur, 443, 553
Drake, J. F., Opher, M., Swisdak, M., & Chamoun, J. N. 2010, ApJ, 709, 963
Harris, E. G. 1962, NCim, 23, 115
Kliem, B. 1994, ApJ, 90, 719
Knizhnik, K., Swisdak, M., & Drake, J. F. 2011, ApJL, 743, L35
Kowal, G., de Gouveia Dal Pino, E. M., & Lazarian, A. 2011, ApJ, 735, 102
Kowal, G., de Gouveia Dal Pino, E. M., & Lazarian, A. 2012, PhRvL, 108, 241102
Kowal, G., Lazarian, A., Vishniac, E. T., & Otmianowska-Mazur, K. 2009, ApJ, 700, 63
Krall, N., & Trivelpiece, A. 1986, Principles of Plasma Physics (San Francisco, CA: San Francisco Press)
Lazarian, A., & Opher, M. 2009, ApJ, 703, 8
Lazarian, A., & Vishniac, E. 1999, ApJ, 517, 700
Lin, R. P., Krucker, S., Hurford, G. J., et al. 2003, ApJL, 595, L69
Liu, Y.-H., Swisdak, M., & Drake, J. F. 2009, PhPl, 16, 042101
Lu, S., Lu, Q., Shao, X., Yoon, P. H., & Wang, S. 2011, PhPl, 18, 072105
McKenzie, D. E., & Savage, S. L. 2009, ApJ, 697, 1569

Øieroset, M., Lin, R. P., Phan, T. D., Larson, D. E., & Bale, S. D. 2002, PhRvL, 89, 195001
Oka, M., Phan, T.-D., Krucker, S., Fujimoto, M., & Shinohara, I. 2010, ApJ, 714, 915
Parker, E. N. 1958, PhRv, 109, 1874
Richardson, J. D., Burlaga, L. F., Decker, R. B., et al. 2013, ApJL, 762, L14
Russell, C. T., & Elphic, R. C. 1979, GeoRL, 6, 33
Sato, T., & Hayashi, T. 1979, PhFl, 22, 1189
Savage, S. L., McKenzie, D. E., & Reeves, K. K. 2012, ApJL, 747, L40
Schoeffler, K. M., Drake, J. F., & Swisdak, M. 2011, ApJ, 743, 70
Shay, M. A., Drake, J. F., Denton, R. E., & Biskamp, D. 1998, JGR, 25, 9165
Sheeley, N. R., Warren, H. P., & Wang, Y.-M. 2004, ApJ, 616, 1224
Simon, J. B., Hawley, J. F., & Beckwith, K. 2009, ApJL, 690, L974
Slavin, J. A., Smith, M. F., Mazur, E. L., et al. 1993, JGR, 98, 15425
Weibel, E. S. 1959, PhRvL, 2, 83